

# Supplementary Information: All-optical mapping of ultrafast carrier dynamics in a Dirac semimetal

Zhaopin Chen,<sup>1,2,3,\*</sup> Camilo Granados,<sup>1,4,5,6,\*</sup> Ido Nisim,<sup>1,2,3</sup> Daniel Kroeger,<sup>1,2,3</sup> Ofer Neufeld,<sup>7</sup> Marcelo F. Ciappina,<sup>1,4,5</sup> and Michael Krüger<sup>1,2,3</sup>

<sup>1</sup>*Department of Physics, Technion – Israel Institute of Technology, Haifa 3200003, Israel*

<sup>2</sup>*Solid State Institute, Technion – Israel Institute of Technology, Haifa 3200003, Israel*

<sup>3</sup>*The Helen Diller Quantum Center,*

*Technion – Israel Institute of Technology, Haifa 3200003, Israel*

<sup>4</sup>*Department of Physics, Guangdong Technion – Israel Institute of Technology, Shantou 515063, Guangdong, China*

<sup>5</sup>*Guangdong Provincial Key Laboratory of Materials and Technologies for Energy Conversion, Guangdong Technion – Israel Institute of Technology, Shantou 515063, Guangdong, China*

<sup>6</sup>*Eastern Institute of Technology, Ningbo 315200, China*

<sup>7</sup>*Schulich Faculty of Chemistry, Technion – Israel Institute of Technology, Haifa 3200003, Israel*

---

\* These authors contributed equally to this work.

## SUPPLEMENTARY TEXT

### Knife-edge measurement of the focus

We characterize the driving laser beam size at the focus using a knife-edge measurement after a parabolic mirror with a focal length of  $f = 25$  mm. As the knife-edge gradually unblocks the beam, the transmitted power increases accordingly, as shown in Fig. S1. Panels **a** and **b** show measurements along the X and Y axes, respectively. The experimental data are fitted using the function:  $P_t(h_i) = P_{\text{offset}} + \frac{P}{2} \text{erfc} \left[ \frac{h_i - h_0}{w/\sqrt{2}} \right]$ , where  $w$  is the  $1/e^2$  beam radius. From the fit, we obtain  $a_x \approx 8.2 \mu\text{m}$  along the X-axis and  $a_y \approx 8.71 \mu\text{m}$  along the Y-axis. The effective beam radius at the focus is then calculated as  $r = \sqrt{a_x a_y} \approx 8.35 \mu\text{m}$ .

### Measured harmonic spectra as functions of $\omega_0 - 2\omega_0$ delay

Experimentally measured harmonic spectra as functions of the two-color delay are presented in Fig. S2, corresponding to Fig. 2 in the main text, but without integrating over specific harmonic energies. Fig. S2a and b show the fourth harmonic from HOPG at peak intensities of 72 and 29  $\text{GW cm}^{-2}$ , respectively, while Fig. S2c displays the sixth harmonic (H6) from ZnO at a peak intensity of 430  $\text{GW cm}^{-2}$  as a reference. For HOPG, it is evident that the time shift corresponding to the maximum harmonic intensity moves to earlier times at higher laser intensities, indicating stronger saturation effects. In contrast, the lower intensity case exhibits much smaller saturation. For ZnO, with its much larger bandgap ( $\sim 3.3$  eV), there is no saturation even at 430  $\text{GW cm}^{-2}$ . Therefore, the maximum harmonic signal consistently appears at zero delay, corresponding to optimal temporal overlap of the fundamental and second harmonic pulses. Additionally, a redshift of the central harmonic energy with increasing delay time is observed.

### Band structure and transition dipole moment of HOPG and ZnO in 1D SBEs

In our one-dimensional semiconductor Bloch equation (SBE) simulations, we model the electronic structure of HOPG by considering only the region near the Dirac cone, with a Fermi velocity of  $V_F = 10^6 \text{ m s}^{-1}$ . Within this linear dispersion regime, the bandgap is given by  $E_g(k) = E_c(k) - E_v(k) = 2V_F|k|$ , and the interband transition dipole moment (TDM)

is defined as  $d_k^{vc} = 1/(2|k|)$ , following Ref.[1] (see Fig.S3). To avoid divergence at  $k = 0$ , we regularize the TDM by introducing a small cutoff, yielding  $d_k^{vc} = 1/(2|k| + \Delta k)$  in our numerical implementation, where  $\Delta k$  corresponds to the discretization step in  $k$ -space.

For ZnO, we use the band structure and transition dipole moment along the  $\Gamma$ -M direction, taken from references [2, 3], as shown in Fig. S4. Here, the ZnO TDM is defined as  $d_k^{vc} = d_0 E_g(0)/E_g(k)$  with  $E_g(k) = E_c(k) - E_v(k)$  and  $d_0 = 3.46$  (a.u.).

### **Interband and intraband harmonics spectra in HOPG**

Figure S5 compares the harmonic spectral intensity contributions from interband and intraband currents in HOPG, driven by a  $2\ \mu\text{m}$  pulse with a peak intensity of  $70\ \text{GW cm}^{-2}$ . The results clearly show that the harmonic yield from the interband current is approximately two orders of magnitude higher than that from the intraband current.

### **SBEs simulated harmonic spectra as functions of $\omega_0 - 2\omega_0$ delay**

Simulated harmonic spectra as functions of the two-color delay, based on the 1D SBEs, are shown in Fig. S6. These correspond to Fig. 2c and d in the main text, but without integration over specific harmonic energies. Fig. S6a and b display the fourth harmonic from HOPG at peak intensities of  $70$  and  $30\ \text{GW cm}^{-2}$ , respectively. Figs. S6c shows the sixth harmonic from ZnO at a peak intensity of  $430\ \text{GW cm}^{-2}$  as a reference.

Compared to the experimental results, the 1D SBE simulations accurately capture the emission time shift corresponding to the maximum harmonic emission ( $\mu_0$ ) in HOPG. The simulations also reveal a redshift in the central harmonic energy as the delay increases, consistent with our experimental observations.

For ZnO, the maximum H6 intensity remains centered around  $\mu_0 = 0$ , indicating negligible saturation effects due to the large bandgap. In addition to the redshift, the H6 spectrum exhibits a clear splitting at larger delays. This feature may arise from interference between different quantum trajectories, such as short and long trajectories, which are likely smeared out in the experiment due to spatial volume averaging.

Since the harmonics generated in HOPG are above the (zero) bandgap and predominantly originate from interband currents, it is more appropriate to compare them with above-

bandgap harmonics in ZnO. Therefore, we use the sixth harmonic from ZnO as a reference, rather than H4, which lies below the bandgap under our two-color excitation conditions.

Nevertheless, we also compare the simulated harmonic intensities of H4, H6, and H8 in ZnO as functions of the two-color delay. Due to the absence of saturation effects, the peak intensities for all three harmonics are centered around zero delay. An exception is H8, which exhibits a slight shift (less than 5 fs) toward positive delay, see Fig. S7.

### **Time-frequency analysis for two-color HHG in HOPG**

To investigate the relationship between single-color and two-color driven HHG in HOPG, we apply a Gabor transform to analyze the time–frequency distribution of the harmonic emission driven by the two-color field at two different delays, as shown in Fig. S8. At a negative delay of  $\tau = -33$  fs, the fourth harmonic exhibits strong emission, primarily localized at negative propagation times that correspond to the delay. In contrast, for a positive delay of  $\tau = 33$  fs, the H4 intensity is significantly weaker and shifts to positive propagation times. These results suggest that the  $2\omega_0$  field acts as a probe, sampling the harmonic emission that originates primarily from the single-color ( $\omega_0$ ) excitation.

### **High harmonics generated from ZnO with an artificially adjusted band gap**

The saturation effect observed in HOPG primarily arises from its gapless band structure, which enables significant electron transitions from the valence to the conduction band. Consequently, similar behavior can be expected in other materials with zero or small band gaps. To explore the influence of the band gap on saturation-induced high-harmonic generation, we artificially reduce the band gap in ZnO and analyze the harmonic emission dynamics using time-frequency (Gabor) analysis. As shown in Fig. S9, a clear shift of the harmonic emission toward earlier times is observed as the band gap decreases. Specifically, the emission time corresponding to the maximum intensity of the fifth harmonic (H5) advances with decreasing band gap, indicating a direct correlation between the band gap size and the saturation-induced temporal shift in harmonic emission.

## Numerical simulation by 2D Semiconductor Bloch equations

To further explore the validity of the simpler 1D SBE numerical approach, we employed a more general 2D SBE simulation performed in the length gauge and in the Houston basis [4]. The numerical approach follows that described in detail in ref. [5], where the equations of motion and procedures can be found. The graphene system is considered with a two-band tight binding Hamiltonian with up to 14 nearest-neighbor hopping terms, which are fitted to density functional theory (DFT) simulations of the ground state bands (following the procedures in ref. [6]). This provides high-accuracy bands around the Dirac cones at  $K$  and  $K'$ . Simulations were performed with a dense  $360 \times 360$   $k$ -grid, using a time step of 4.8 as and following the experimental conditions. We employed a  $T_2$  value of 6.6 fs, similar to the 1D model, and also tested longer  $T_2$  of 25 fs. The harmonic yield was integrated around the peak without any filtration and calculated vs. two-color delay in steps of  $\sim 1.5$  fs.

The 2D SBE simulations yielded qualitatively similar results (see Fig. S10a) to the 1D case, i.e. there was a negative time shift for two-color delay leading to the maximum emission of the 4th harmonic. This result justifies applying the simpler model that is easier to analyze and is much more numerically tractable. We also note that we found the 2D model much more sensitive to  $T_2$  dephasing time, whereby longer dephasing times caused the maximizing two-color delay to shift to positive values (see Fig. S10b). This did not occur in the 1D model, or under any conditions in our experiments, and we believe might be a result of the  $T_2$  phenomenological dephasing being a bad approximation in our conditions (where the total simulation duration far exceeds several tens of femtoseconds and either k-dependent dephasing[7] or electron-phonon dynamics might be required [8]).

## DFT-calculated band structures of graphene and HOPG

Here, we present the electronic band structures of graphene and HOPG along high-symmetry paths, as shown in Fig. S11, calculated using first-principles DFT (following the procedures in ref. [6]). Notably, HOPG exhibits a Dirac cone-like dispersion near the  $H$  point, analogous to the well-known Dirac cone at the  $K$  or  $K'$  point in monolayer graphene. However, in AB-stacked HOPG, interlayer coupling breaks the original symmetry of the monolayer, leading to a distortion and partial lifting of the Dirac cone structure.

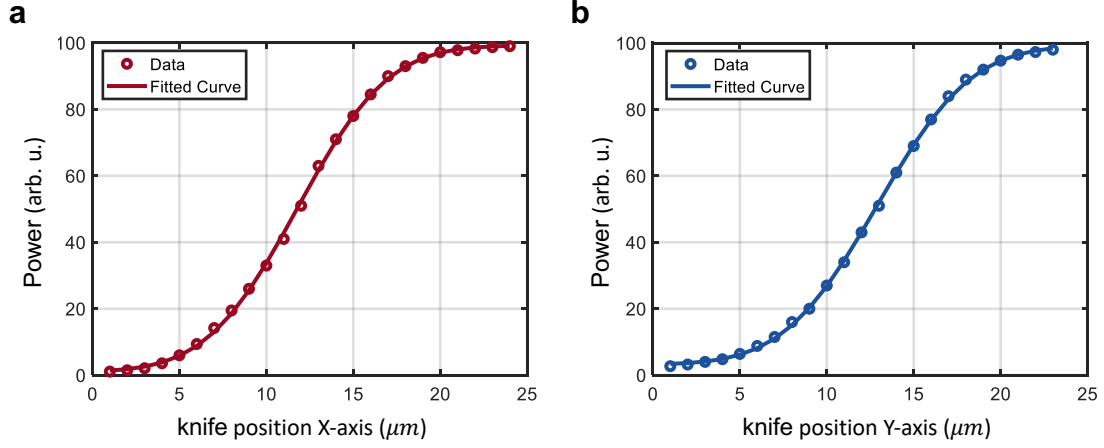


Figure S1. Knife-edge measurement of the beam size at the focus. The transmitted power is fitted using the function  $P_t(h_i) = P_{\text{offset}} + \frac{P}{2}, \text{erfc} \left[ \frac{h_i - h_0}{w/\sqrt{2}} \right]$ , where  $w$  denotes the  $1/e^2$  beam radius. From the fit, we obtain  $a_x \approx 8.2 \mu\text{m}$  along the X-axis and  $a_y \approx 8.71 \mu\text{m}$  along the Y-axis. The effective beam radius at the focus is therefore  $r = \sqrt{a_x a_y} \approx 8.35 \mu\text{m}$ .

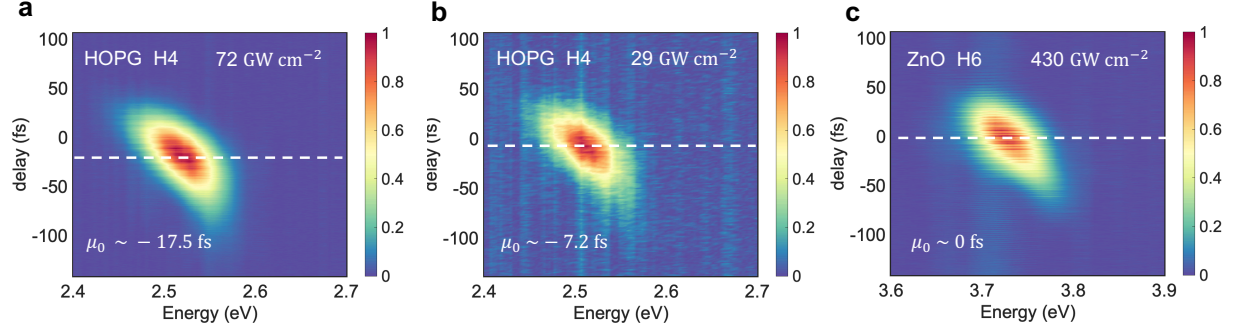


Figure S2. Experimentally measured harmonic spectra as functions of the two-color delay, corresponding to Fig. 2 in the main text. **a** and **b**, Fourth harmonic (H4) from HOPG at peak intensities of 72 and 29 GW cm<sup>-2</sup>, respectively. **c**, sixth harmonic (H6) from ZnO at a peak intensity of 430 GW cm<sup>-2</sup>. The white dashed lines indicate the delay times corresponding to the maximum harmonic intensities.

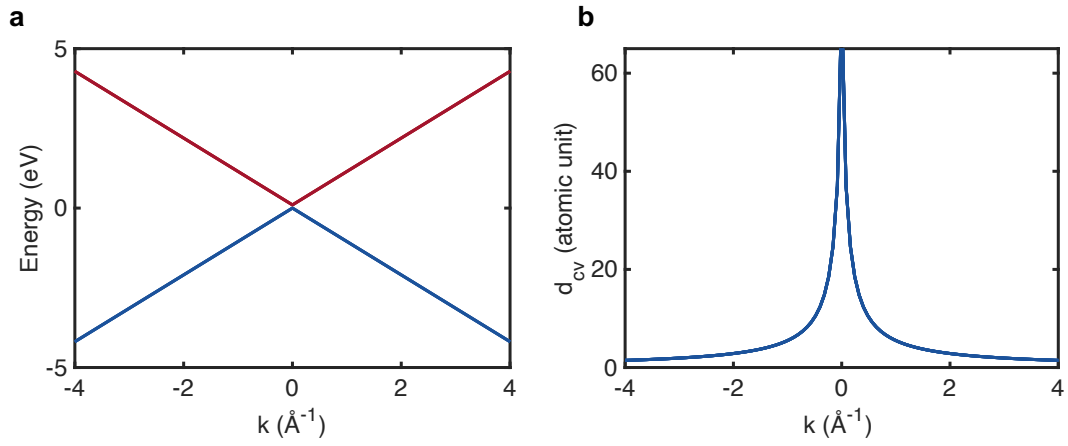


Figure S3. **a**, One-dimensional band structure and **b**, transition dipole moment of graphene-like HOPG around Dirac cone used in the SBE calculations.

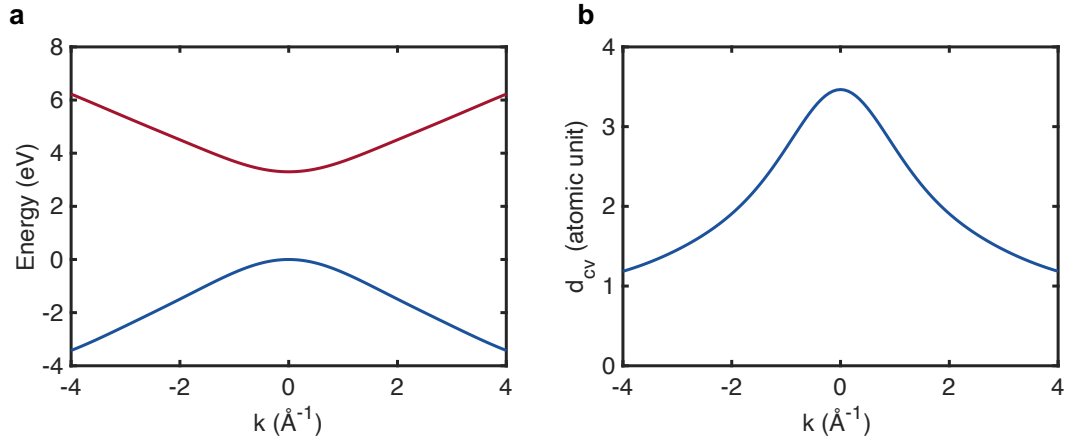


Figure S4. **a**, One-dimensional band structure and **b**, transition dipole moment of ZnO along  $\Gamma-M$  orientation used in the SBE calculations.

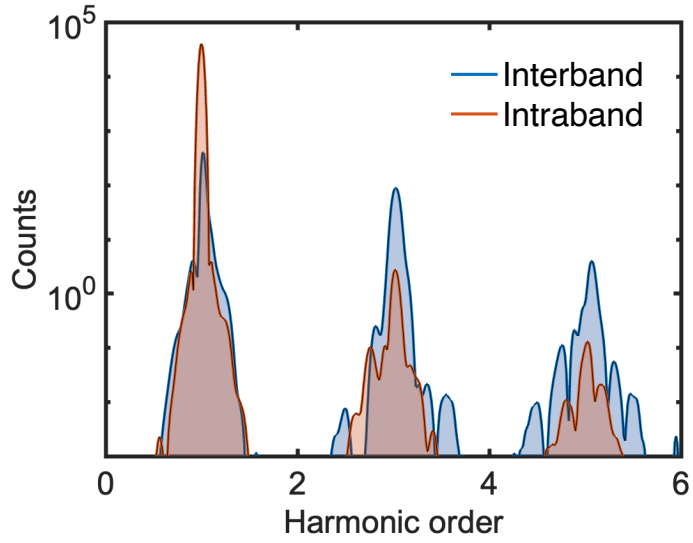


Figure S5. Harmonic spectra simulated using the semiconductor Bloch equations (Eqs. (1) in the main text), driven solely by a 1980 nm laser pulse at a peak intensity of  $70 \text{ GW cm}^{-2}$  in HOPG. The interband harmonics clearly dominate, with intensities approximately two orders of magnitude higher than the intraband harmonics.

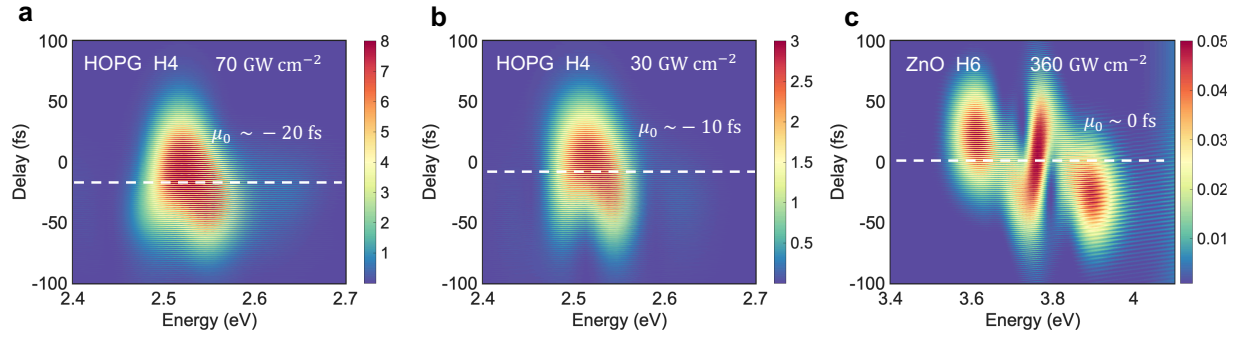


Figure S6. SBEs simulated harmonic spectra as functions of the two-color delay, corresponding to Fig. 2 in the main text: (a, b) fourth harmonic (H4) from HOPG at peak intensities of 70 and 30 GW cm<sup>-2</sup>, respectively; (c) sixth harmonic (H6) from ZnO at a peak intensity of 430 GW cm<sup>-2</sup>. The white dashed lines indicate the delay times corresponding to the maximum harmonic intensities.

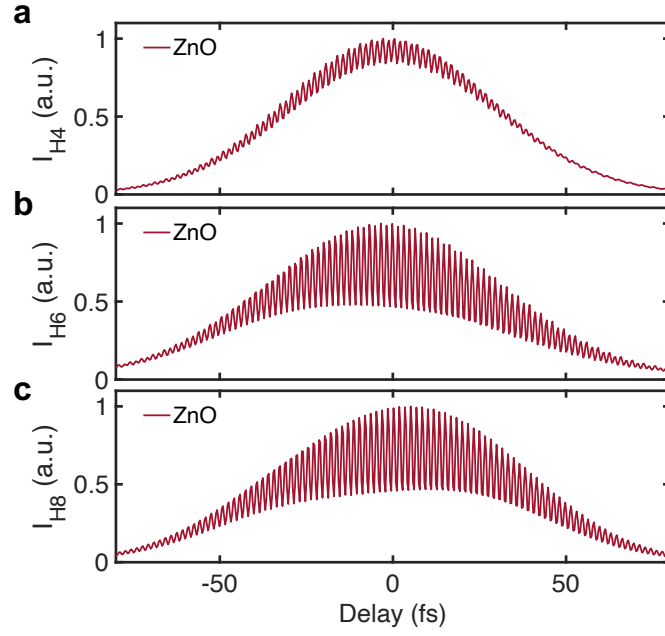


Figure S7. Simulated harmonic intensities in ZnO as functions of the  $\omega_0-2\omega_0$  time delay for (a) the 4th harmonic (H4), (b) the 6th harmonic (H6), and (c) the 8th harmonic (H8), respectively.

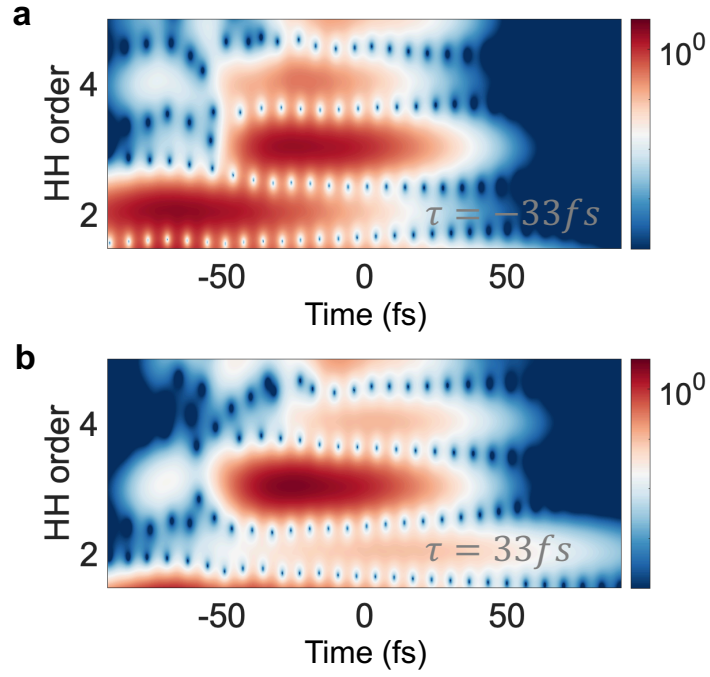


Figure S8. Gabor transform of the harmonic emission generated by  $\omega_0-2\omega_0$  two-color pulses at different delay times: (a)  $\tau = -33, fs$  and (b)  $\tau = 33, fs$ . The driving laser intensity is fixed at  $70 \text{ GW cm}^{-2}$ .

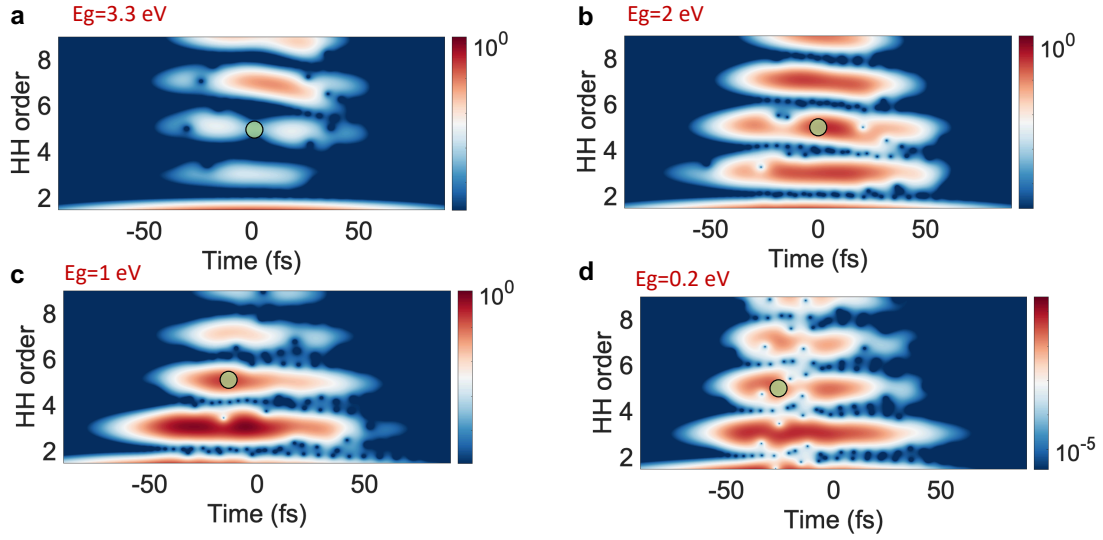


Figure S9. Time-frequency analysis of interband harmonics using a Gabor transformation at a 1980 nm peak intensity of  $I = 430 \text{ GW cm}^{-2}$ . The maximum intensity of the harmonics is shown for ZnO with manually adjusted bandgaps: **a**  $E_g = 3.3 \text{ eV}$ , **b**  $E_g = 2.0 \text{ eV}$ , **c**  $E_g = 1.0 \text{ eV}$ , and **d**  $E_g = 0.2 \text{ eV}$ . A clear shift to negative emission times is observed as the bandgap decreases, indicating earlier saturation of the valence band due to more easily driven interband transitions in narrower-gap materials.

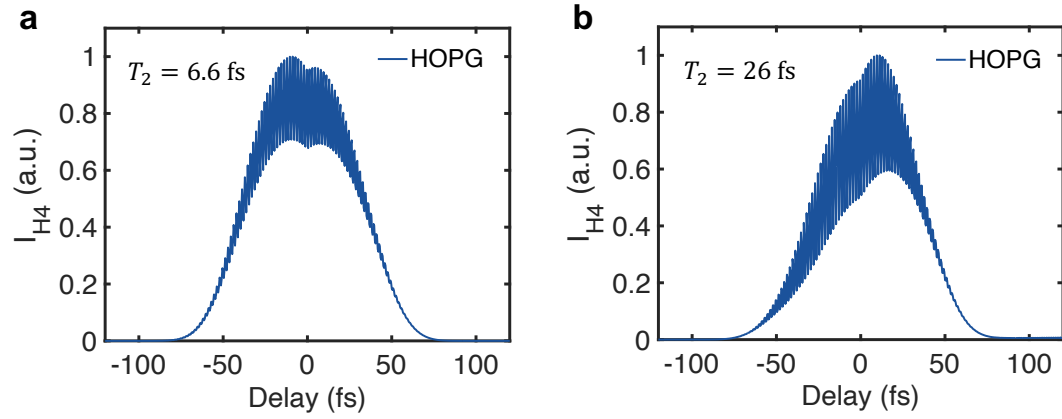


Figure S10. Fourth harmonic intensity in HOPG as a function of the  $\omega_0-2\omega_0$  time delay, simulated using two-dimensional SBEs. **a** With an interband decoherence time of  $T_2 = 6.6$  fs, a slight negative shift in the delay corresponding to the maximum signal is observed. **b** With a longer decoherence time of  $T_2 = 26$  fs, the maximum shifts slightly to positive delay (unlike the exp. result).

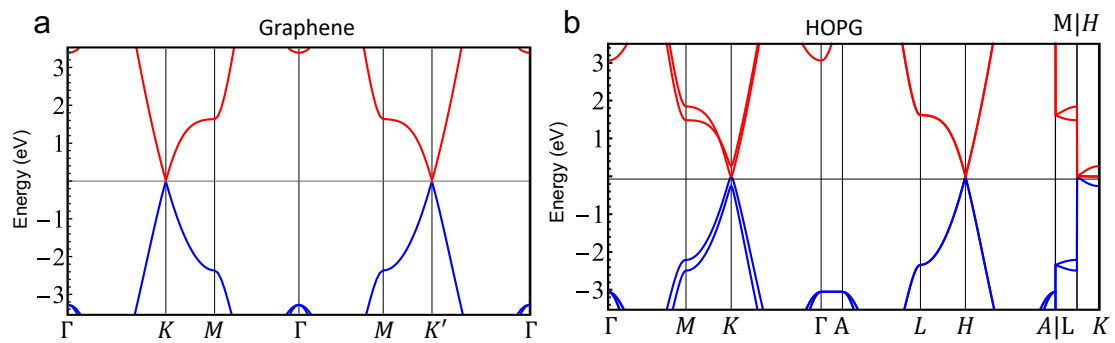


Figure S11. DFT-calculated electronic band structures along high-symmetry directions. **a**, Monolayer graphene; **b**, Highly oriented pyrolytic graphite (HOPG).

- 
- [1] Al-Naib, I., Sipe, J. E. & Dignam, M. M. High harmonic generation in undoped graphene: Interplay of inter- and intraband dynamics. *Phys. Rev. B* **90**, 245423 (2014).
- [2] Vampa, G., McDonald, C. R., Orlando, G., Corkum, P. B. & Brabec, T. Semiclassical analysis of high harmonic generation in bulk crystals. *Phys. Rev. B* **91**, 064302 (2015).
- [3] Yu, C., Zhang, X., Jiang, S., Cao, X., Yuan, G., Wu, T., Bai, L. & Lu, R. Dependence of high-order-harmonic generation on dipole moment in SiO<sub>2</sub> crystals. *Phys. Rev. A* **94**, 013846 (2016).
- [4] Yue, L. & Gaarde, M. B. Introduction to theory of high-harmonic generation in solids: tutorial. *J. Opt. Soc. Am. B* **39**, 535–555 (2022).
- [5] Kim, M., Kim, T., Galler, A., Kim, D., Chacon, A., Gong, X., Yang, Y., Fang, R., Watanabe, K., Taniguchi, T., Kim, B. J., Chae, S. H., Jo, M.-H., Rubio, A., Nuefeld, O. & Kim, J. Quantum interference and occupation control in high harmonic generation from monolayer WS<sub>2</sub>. *arXiv preprint arXiv:2503.04335* (2025).
- [6] Nuefeld, O., Hübener, H., Jotzu, G., De Giovannini, U. & Rubio, A. Band nonlinearity-enabled manipulation of Dirac nodes, Weyl cones, and valleytronics with intense linearly polarized light. *Nano Lett.* **23**, 7568–7575 (2023).
- [7] Korolev, V., Lettau, T., Krishna, V., Croy, A., Zuerch, M., Spielmann, C., Waechtler, M., Peschel, U., Graefe, S., Soavi, G. & Kartashov, D. Unveiling the role of electron-phonon scattering in dephasing high-order harmonics in solids. *arXiv preprint arXiv:2401.12929* (2024).
- [8] Lively, K., Sato, S. A., Albareda, G., Rubio, A. & Kelly, A. Revealing ultrafast phonon mediated inter-valley scattering through transient absorption and high harmonic spectroscopies. *Phys. Rev. Research* **6**, 013069 (2024).

# All-optical mapping of ultrafast carrier dynamics in a Dirac semimetal

Zhaopin Chen,<sup>1,2,3,\*</sup> Camilo Granados,<sup>1,4,5,6,\*</sup> Ido Nisim,<sup>1,2,3</sup> Daniel Kroeger,<sup>1,2,3</sup> Ofer Neufeld,<sup>7</sup> Marcelo F. Ciappina,<sup>1,4,5</sup> and Michael Krüger<sup>1,2,3</sup>

<sup>1</sup>*Department of Physics, Technion – Israel Institute of Technology, Haifa 3200003, Israel*

<sup>2</sup>*Solid State Institute, Technion – Israel Institute of Technology, Haifa 3200003, Israel*

<sup>3</sup>*The Helen Diller Quantum Center,*

*Technion – Israel Institute of Technology, Haifa 3200003, Israel*

<sup>4</sup>*Department of Physics, Guangdong Technion – Israel Institute of Technology, Shantou 515063, Guangdong, China*

<sup>5</sup>*Guangdong Provincial Key Laboratory of Materials and Technologies for Energy Conversion, Guangdong Technion – Israel Institute of Technology, Shantou 515063, Guangdong, China*

<sup>6</sup>*Eastern Institute of Technology, Ningbo 315200, China*

<sup>7</sup>*Schulich Faculty of Chemistry, Technion – Israel Institute of Technology, Haifa 3200003, Israel*

## Abstract

High-harmonic generation (HHG), the hallmark effect of attosecond science, is a nonperturbative nonlinear process leading to the emission of high harmonic light from gases and solids. In gases, extreme driving laser pulse intensities can deplete the ground state, suppressing harmonic emission during the trailing edge of the pulse. Here, we report pronounced ultrafast depletion dynamics during HHG in a gapless Dirac semimetal—highly oriented pyrolytic graphite (HOPG). Remarkably, HOPG supports nonperturbative harmonic generation at laser intensities as low as  $10^{10} \text{ W cm}^{-2}$ , facilitated by its vanishing bandgap. Using two-color spectroscopy, we reveal the excitation dynamics of Dirac electron-hole pairs as it affects the emission of harmonics during the presence of the driving laser pulse. Notably, valence band depletion near the Dirac points leads to a marked suppression of interband harmonics and induces measurable temporal shifts. These observations are supported by simulations based on semiconductor Bloch equations. Our findings uncover a new regime of strong-field light–matter interaction in gapless solids and establish HHG as a sensitive, all-optical probe of ultrafast carrier dynamics, offering new opportunities for ultrafast optoelectronics in Dirac materials.

## MAIN

Parametric nonlinear optical processes, such as second-harmonic generation or four-wave mixing, transiently modify the quantum state of a medium during the laser interaction, but leave it unchanged afterward<sup>1</sup>. This framework extends even to high-harmonic generation (HHG), an extreme nonlinear strong-field-driven process observed mainly in gases<sup>2–4</sup> and condensed-matter systems<sup>5–9</sup>, which cannot be described by perturbative nonlinear optics. Although HHG itself is parametric, competition with other strong-field processes can affect HHG, most prominently photoionization<sup>4</sup>. In gases, sufficiently intense and long laser pulses can substantially deplete the ground-state electron population, suppressing harmonic emission, causing spectral shifts and reducing harmonic cutoff energies<sup>10,11</sup>. Additionally, the resulting high densities of photoelectrons adversely affect harmonic phase matching<sup>12,13</sup>.

---

\* These authors contributed equally to this work.

In solids, analogous depletion phenomena might be expected at considerably lower laser intensities due to their smaller bandgaps relative to atomic ionization energies. However, experimental observation of pronounced depletion dynamics during solid-state HHG remains elusive. Achieving a significant suppression of harmonic emission typically requires excitation fractions on the order of  $\sim 40\%$ , while in experiment, typical excitation levels in semiconductors are usually limited to a few percent to avoid material damage<sup>14</sup>. Pre-excitation of carriers with ultraviolet pulses has been explored as an alternative route to reach the depletion regime and suppress the HHG yield in semiconductors<sup>14–16</sup>. However, such approaches obscure the intrinsic depletion dynamics driven solely by the fundamental laser pulse which drives the HHG process. Here, the subject of depletion and HHG yield suppression is an intricate one because condensed matter is far more complex than the gas phase due to its strong multi-electron nature, lower symmetry, and Bloch state delocalization. Moreover, the microscopic origins of harmonic suppression in solids remain actively debated. Suppression could arise predominantly from Pauli blocking, where transitions from valence to conduction bands become unavailable due to occupied states, or from excitation-induced dephasing, where increased carrier densities accelerate electron scattering and degrade interband coherence<sup>17</sup>.

Highly oriented pyrolytic graphite (HOPG), a structurally robust carbon-based bulk material composed of stacked graphene layers<sup>18,19</sup>, provides a promising platform for investigating such intrinsic depletion dynamics under strong-field driving. HOPG retains the key electronic properties of monolayer graphene, including its gapless Dirac dispersion, high carrier mobility, and strong anisotropic optical responses<sup>20–22</sup>. It also offers additional experimental advantages, such as structural robustness and scalability, that overcome the intrinsic limitation of graphene’s low damage threshold. Furthermore, HOPG allows systematic exploration of the effects of interlayer coupling and thickness variations on nonlinear optical and electronic dynamics<sup>23</sup>. Despite these compelling features, HHG in HOPG remains experimentally unexplored to date.

In this combined experimental and theoretical study, we introduce an all-optical two-color spectroscopy technique to track population dynamics in the Dirac cone, revealing behavior beyond that observed in conventional gapped solids. Specifically, we observe a time shift in harmonic emission relative to the driving field peak, a clear signature of strong-field-induced depletion in a gapless Dirac semimetal. While prior studies have investigated photon-induced

saturation in graphene for applications, such as saturable absorbers<sup>24</sup>, our work explores a fundamentally distinct regime, the nonperturbative strong-field limit, where carrier depletion evolves within a few optical cycles and directly influences HHG. This bridges the gap between weak-field saturation effects and strong-field dynamics in Dirac materials, uncovering a new class of ultrafast phenomena governed by light-driven population reshaping. More broadly, the ability to resolve femtosecond-scale carrier depletion through HHG suppression suggests that this approach could also serve as a sensitive, all-optical probe of light-induced phase transitions in solids<sup>25–27</sup>.

## RESULTS

### Nonperturbative harmonic generation in HOPG

We generate high harmonics from an HOPG sample in reflection geometry<sup>28</sup> using an infrared femtosecond pulse (frequency  $\omega_0$ ) combined with a weak, synchronized second harmonic (SH) field ( $2\omega_0$ ), with a polarization parallel to the fundamental pulse (see Fig. 1a). The fundamental pump pulse has a central wavelength of 1980 nm and a duration of 60 fs (about 10 optical cycles). The SH field is generated by focusing the fundamental field onto a  $\beta$ -barium borate (BBO) crystal. Both beams are split and then recombined in an interferometric setup, achieving both spatial and temporal overlap with accurate control of the two-color ( $\omega_0-2\omega_0$ ) time delay  $\tau$  (see Methods). Throughout this work, we set the SH pulse intensity at 3% of the fundamental pump intensity in both the experimental measurements and theory calculations.

HOPG exhibits an AB-stacked multilayer graphene structure, resulting in a stable crystalline form whose band dispersion near the Dirac point closely resembles that of monolayer graphene. For comparison, *ab initio* calculations of the electronic band structures of both graphene and HOPG are provided in Fig. S11 of the Supplementary Information. Given the moderate pump field strength used in our experiments – limited by the damage threshold of the material – the electron dynamics are effectively confined to the vicinity of the Dirac cone (Fig. 1b). In the nonperturbative regime relevant to our work, the emission of above-bandgap harmonics is primarily governed by interband polarization processes. This behavior is further corroborated by numerical simulations based on the semiconductor Bloch equa-

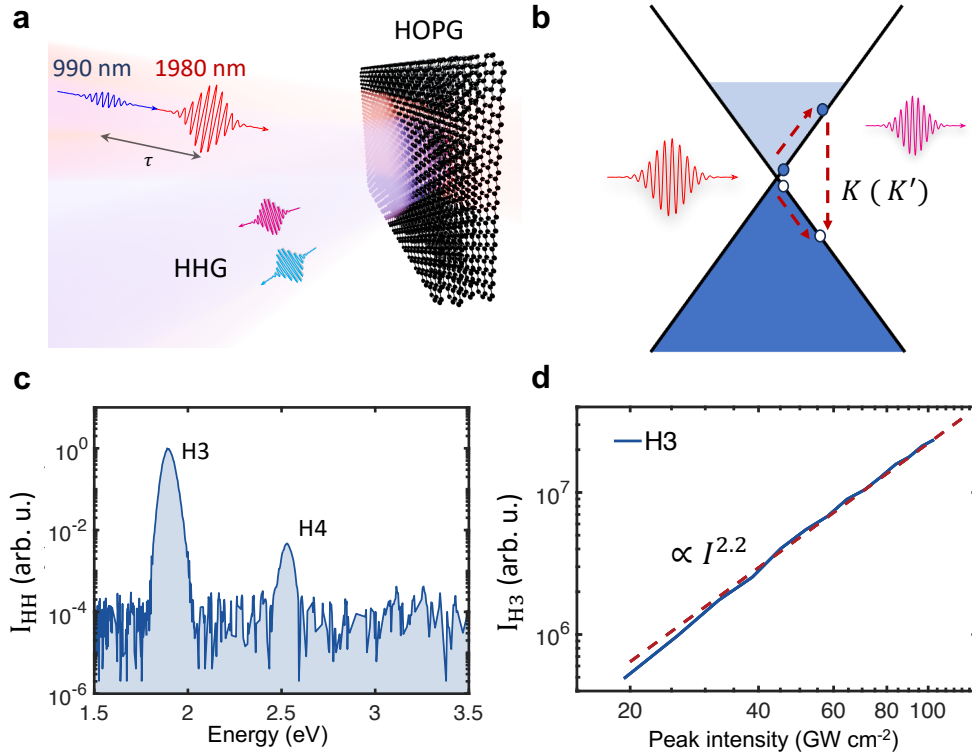


Figure 1. **High-harmonic generation from HOPG by a two-color pulse.** **a**, Conceptual sketch of high-harmonic generation in HOPG driven by a strong driving laser pulse with 1980 nm central wavelength and a weak second harmonic pulse. **b**, Three-step model of interband HHG around the Dirac cone. **c**, Experimentally measured harmonic spectrum with a laser peak intensity of  $72 \text{ GW cm}^{-2}$  and 3% second harmonic admixture. **d**, Intensity scaling of the third harmonic yield  $I_{H3}$  when driven by the fundamental pulses only. The strong deviation of the observed scaling ( $\propto I^{2.2}$ ) from the expected three-photon scaling ( $\propto I^3$ ) places our experiment in the non-perturbative regime of HHG.

tions (SBEs), which reveal a clear predominance of interband contributions in the generated harmonic spectrum (see Fig. S5 in Supplementary Information). Interband polarization roughly corresponds to the three-step picture of HHG. Here, interband tunneling produces an electron-hole pair that is driven by the laser field in momentum space until electron and hole recombine and a harmonic photon is emitted<sup>6</sup>.

In our experiment, non-perturbative high harmonics are generated from HOPG with spectral features observed up to the fourth order (2.5 eV photon energy) near the reported harmonic cutoff in monolayer graphene around 2.4 eV<sup>29,30</sup>. Figure 1c displays the mea-

sured harmonic spectrum obtained using the 1980 nm driving pulse with a peak intensity of  $72 \text{ GW cm}^{-2}$  and the admixed SH pulse. With respect to the third harmonic, the fourth harmonic exhibits a relative intensity of  $I_{\text{H4}}/I_{\text{H3}} = 6.3\%$ , while the second harmonic is omitted from the spectrum, as it is masked by the much more intense incident SH field.

To confirm the nonperturbative nature of the harmonic emission, we measure the intensity scaling of the third harmonic (H3) driven by a single-color 1980 nm pulse (Fig. 1d). The third harmonic exhibits a power-law dependence of approximately  $I^{2.2}$ , deviating from the expected perturbative scaling of  $I^3$  and confirming the involvement of strong-field electron-hole dynamics. This nonlinear response arises from electron-hole acceleration and recombination processes rather than multiphoton transitions, underscoring that our measurements are firmly within the non-perturbative regime.

### **Emission time shift of harmonic generation**

Two-color spectroscopy is a powerful all-optical approach capable of retrieving the temporal dynamics of the harmonic emission all the way down to the sub-cycle scale<sup>31</sup>. Here, we measure the harmonic intensity as a function of the relative time delay  $\tau$  between the two colors ( $\omega_0-2\omega_0$ ), as shown in Fig. 2. The fourth harmonic (H4) is generated in HOPG when the  $\omega_0$  and  $2\omega_0$  pulses temporally overlap, enabled by symmetry breaking of the fundamental  $\omega_0$  electric field through perturbation by the  $2\omega_0$  pulse (Fig. 2a). As a reference, we replace the HOPG sample with a conventional bulk gapped solid HHG sample, a ZnO crystal<sup>5,6</sup>, and measure the above-band gap sixth harmonic (H6) intensity as a function of  $\tau$ . The measurements in ZnO are performed under the same conditions as in HOPG, except that the fundamental pump intensity is increased to  $384 \text{ GW cm}^{-2}$  to ensure the generation of above-band gap harmonics through the interband process. The band gap of the ZnO crystal is around 3.3 eV. Full delay-dependent harmonic spectra are shown in Fig. S2 of the Supplementary Information.

In each of plots shown in Fig. 2, oscillations of the harmonic signal with a frequency of  $4\omega_0$  are visible on top of an overall Gaussian-like curve. In our work, we focus on the latter. Remarkably, we observe that the maximum signal of H4 in HOPG occurs approximately  $17.5 \pm 0.2$  fs before the temporal overlap of the two pulse intensity peaks at  $\tau = 0$ . In contrast, the H6 signal in ZnO exhibits a symmetric delay dependence, with its maximum occurring

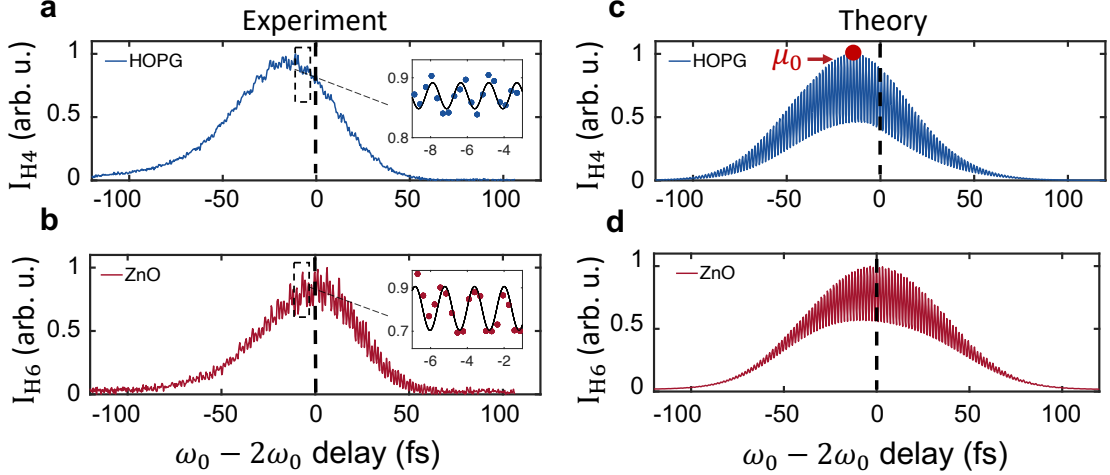


Figure 2. **Harmonic intensity as a function of  $\omega_0-2\omega_0$  delay.** **a**, Experimentally measured harmonic intensities as function of the  $\omega_0-2\omega_0$  delay for the fourth harmonic (H4) in HOPG with  $\omega_0$  peak intensity  $72 \text{ GWcm}^{-2}$ . **b**, The same for the sixth harmonic (H6) in ZnO with pump intensity  $430 \text{ GWcm}^{-2}$ . **c** and **d**, Corresponding theoretical results simulated based on the semiconductor Bloch equations (Eq. 1) for comparison with the experimental data of HOPG and ZnO, respectively. Note that for negative delays, the  $2\omega_0$  pulse arrives earlier at the HHG medium than the  $\omega_0$  pulse. The peak emission of H4 occurs approximately  $17.5 \pm 0.2$  fs before the optimal temporal overlap in the experiment and 17.7 fs in the simulation.

precisely at zero delay. The time shift  $\mu_0$  corresponding to the maximum harmonic signal is extracted by fitting the entire delay-dependent harmonic trace with a Gaussian function and identifying the peak position of the fit. To gain further insight into the underlying physics, we perform theoretical simulations based on both one-dimensional (1D) and two-dimensional (2D) semiconductor Bloch equations (SBEs, see Methods in the main text and Supplementary Information for details) using the same parameters as in the experiment for both HOPG and ZnO (Fig. 2c and d; see also full spectra in Fig. S6 of the Supplementary Information). Under a fixed interband decoherence time of  $T_2 = 6.6$  fs, both the 1D and 2D models exhibit a negative delay for the harmonic maximum (note that the negative delay in 2D simulation is sensitive to the choice of  $T_2$ ). Since the 1D SBE model reproduces the main features observed in the 2D simulations, including the negative time shift of the harmonic maximum, we adopt the simpler 1D model for the remainder of our analysis. The simulation results show excellent agreement with the experimental data. We accurately reproduce the

time shift of the H4 signal in HOPG, yielding a similar shift  $\mu_0 = -17.7$  fs with respect to  $\tau = 0$ , and correctly predict the peak of the H6 signal in ZnO at zero delay. Furthermore, we simulate the delay dependence of H4, H6, and H8 from ZnO, and in all cases, the harmonic maxima occur near  $\tau = 0$ , confirming that the choice of H6 as a reference does not affect the evaluation of the delay.

To gain deeper insight into the pronounced time shift observed in HHG from HOPG, we analyze the time evolution of both the conduction band electron population  $f_c(k, t)$  and the interband polarization  $p(k, t)$ , as shown in Figs. 3a and b. Our calculations reveal that this shift originates from the strong interplay between intraband and interband currents in the gapless Dirac cone. A significant accumulation of intraband population leads to a suppression of the interband polarization. Notably, the conduction band population near the Dirac point rapidly approaches half-filling well before the peak of the driving field, indicating a pronounced saturation effect. Unlike conventional solid-state HHG processes where depletion is negligible<sup>32</sup>, the time-dependent  $k$ -space populations  $f_k^{c,v}(t)$  of conduction ( $c$ ) and valence ( $v$ ) bands play a crucial role in the interband transition term  $(1 - f_k^c(t) - f_k^v(t)) d_k^{c\nu} E(t)$  in the SBEs (see the Methods section, Eq. (1)). Once both  $f_k^c$  and  $f_k^v$  reach 0.5, the interband transition term vanishes, effectively blocking further interband excitation – a phenomenon known as Pauli blocking. This behavior is analogous to a two-level system where population inversion is forbidden and the excitation process saturates due to balanced electron occupation across bands.

The inability of the conduction band population to significantly exceed half-filling for most  $k$ -points around the Dirac point indicates that saturation occurs early during the fundamental driving pulse. This saturation not only limits further excitation, but also suppresses the interband polarization, which is an essential ingredient for interband HHG. As a result, the dominant interband term is weakened, even near the peak of the driving pulse. Instead, the maximum interband harmonic intensity occurs prior to the onset of saturation.

To visualize this effect more clearly, we compute the *total* conduction band population (around the cone) by integrating over momentum space,  $n_c(t) = \int f_c(k, t) dk$ , shown in Fig. 3c. It is evident that the excitation of 50% of the final total population (which remains after the end of the laser pulse) is achieved at a significantly earlier time than the peak of the driving field, underscoring the presence of strong saturation and depletion. In the absence

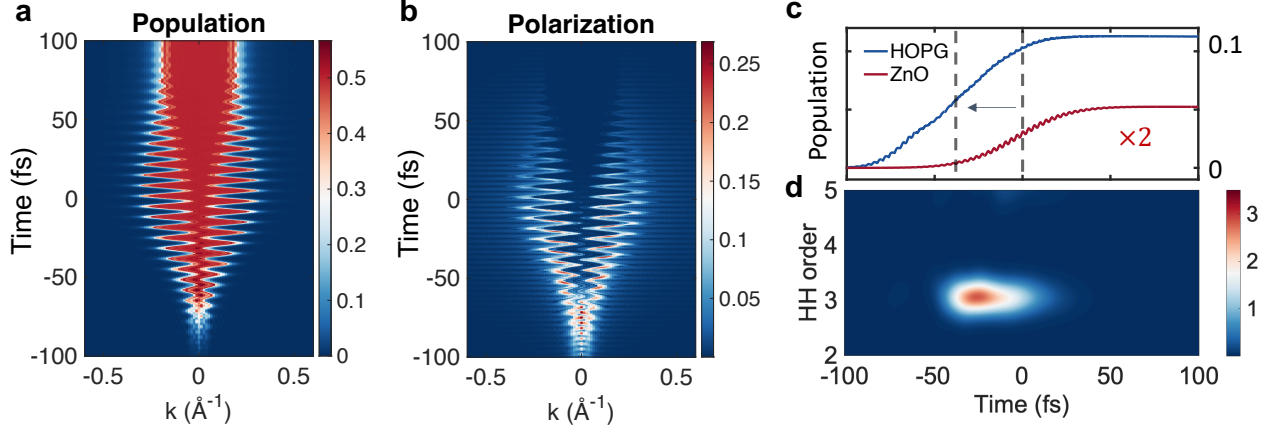


Figure 3. **Carrier depletion dynamics around Dirac points.** **a**, Calculated conduction band electron population dynamics and **b**, interband polarization dynamics in momentum space during the excitation driven solely by the fundamental pulse at an intensity of  $72 \text{ GW cm}^{-2}$ . In the gapless Dirac cone, carrier populations can reach up to 50% at each  $k$ -point, leading to pronounced depletion effects. **c**, The total conduction band population dynamics show that the excitation of 50% of the final population occurs well before the peak of the driving field. For comparison, the HHG process in ZnO at a peak intensity of  $430 \text{ GW cm}^{-2}$  shows that the excitation of 50% of the final population coincides with the peak of the laser pulse. **d**, Time-frequency analysis of the interband harmonics using a Gabor transform reveals that the maximum intensity of the third harmonic (H3) occurs prior to the peak of the driving field.

of depletion, one would expect this time to coincide with the peak of the driving field due to its temporal symmetry. For comparison, we also plot the calculated total conduction band population dynamics in ZnO, which shows that the excitation of 50% of the final total population occurs right at the peak field, consistent with the larger band gap that prevents efficient depletion.

Furthermore, a time-frequency analysis using a Gabor transform (Fig. 3d) shows that the maximum intensity of the H3 in HOPG driven by a single-color  $2 \mu\text{m}$  pulse occurs approximately 25 fs before the field maximum ( $t = 0$ ). A complementary Gabor transform of the harmonic emission driven by  $\omega_0 - 2\omega_0$  two-color pulses at various time delays (see Fig. S8 in the Supplementary Information) demonstrates that the  $2\omega_0$  field primarily acts as a probe, sampling the harmonic emission originating from the single-color  $\omega_0$  excitation. This is in contrast to wide-band gap semiconductors where the non-depletion approximation

is valid and interband polarization is largely unaffected by intraband population. In our case, the absence of a band gap in HOPG leads to substantial carrier excitation around the Dirac cone and strongly modifies the interband contribution to HHG. Consequently, intraband population dynamics play a critical role in shaping the overall HHG process in gapless Dirac materials such as HOPG. One can also expect to see a strong saturation effect in wide-bandgap semiconductor HHG as long as the pump intensity is sufficiently large. However, the low damage threshold of these materials prevents a clear observation of this effect in gapped solids. Nonetheless, our simulations confirm that the harmonic emission time shifts significantly earlier even in ZnO when its band gap is artificially reduced in simulations to a nearly gapless regime, as shown in Fig. S9 of the Supplementary Information.

Since the emission time shift originates from dynamic population saturation, a stronger driving laser intensity is expected to induce earlier saturation during the driving process. To investigate this, we experimentally measure the time shift of H4 under various  $\omega_0$  pump intensities, as shown in Fig. 4a. As the driving laser intensity increases, the peak of the H4 signal in the  $\omega_0$ - $2\omega_0$  delay scan systematically shifts to earlier times, further corroborating the presence of a saturation effect. The relationship between the H4 emission time shift  $\mu_0$  and the driving laser intensity is plotted in Fig. 4b.

Our SBE-based simulations accurately reproduce the experimental trend, confirming that the negative time shift  $\mu_0$  increases with increasing peak intensity. To gain further insight into the phenomenon, we introduce an analytical approximation (Eqs. 8–12) based on Fermi’s golden rule, assuming non-depleted excitation from the valence band to the conduction band while accounting for the influence of electron occupation in both bands on the excitation rate. This model also predicts a similar dependence of  $\mu_0$  on the pump intensity, as indicated by the black dashed line in Fig. 4b.

### **Dirac electron population dynamics**

Because the time shift of the maximum harmonic intensity induced by saturation is highly sensitive to the electron population, it can serve as an effective probe for tracking electron population dynamics. To investigate this, we analyze the electron dynamics associated with H4 generation through the interband process by integrating the conduction band population over the momentum-space region where the bandgap energy corresponds to the H4 photon

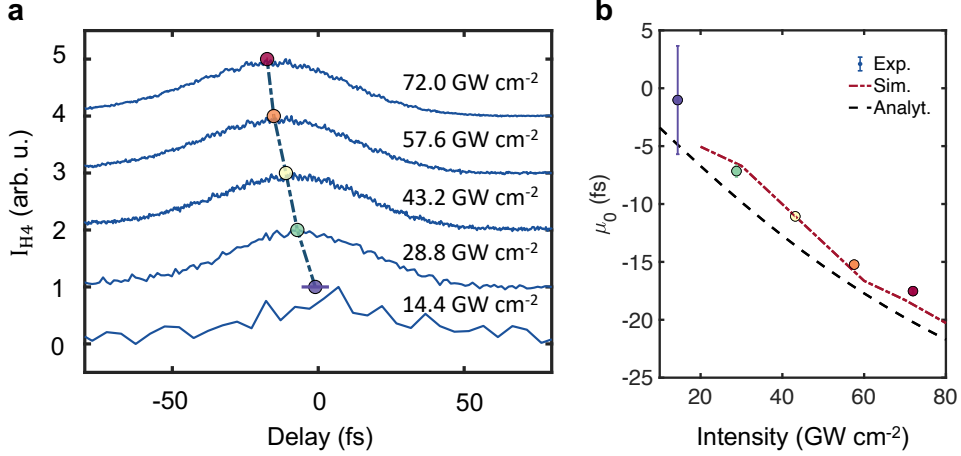


Figure 4. **H4 emission time shift as a function of pump intensity.** **a**, Experimentally measured normalized H4 intensity as a function of  $\omega_0-2\omega_0$  delay at different pump intensities. The relative delay position ( $\mu_0$ ) of the maximum H4 intensity shifts to earlier times as the pump intensity increases. For better visibility, we introduce horizontal offsets. **b**, Comparison of the maximum H4 intensity delay as a function of  $\omega_0$  pump intensity obtained from experimental measurements, SBE calculations, and analytical results based on Eq. 12. Experimental uncertainties for  $\mu_0$  are smaller than the marker size at higher intensities.

energy (see Fig. 5a).

Under excitation by a  $2 \mu\text{m}$  pulse with a peak intensity of  $70 \text{ GW cm}^{-2}$ , the electron population contributing to H4 exhibits strong temporal oscillations (see Fig. 5b). We define  $t_c$  as the time at which half of the electrons in this momentum-space region have transitioned to the conduction band. As shown in Fig. 5c, the absolute value of  $t_c$  increases with pump intensity, indicating an intensity-dependent excitation process. Furthermore, a strong correlation is observed between  $t_c$  (in the single-color  $2 \mu\text{m}$  excitation case) and  $\mu_0$  (emission time shift corresponding to the maximum H4 intensity in the two-color excitation case). The correspondence can be captured by a second-order polynomial fitting function,  $t_c = 0.027\mu_0^2 + 0.63\mu_0 - 16.71$ , with an  $R^2$  value of 0.99, indicating very strong correlation between these two physical observables. This demonstrates an all-optical method for probing carrier population dynamics in Dirac materials and semi-metallic systems under strong-field excitation.

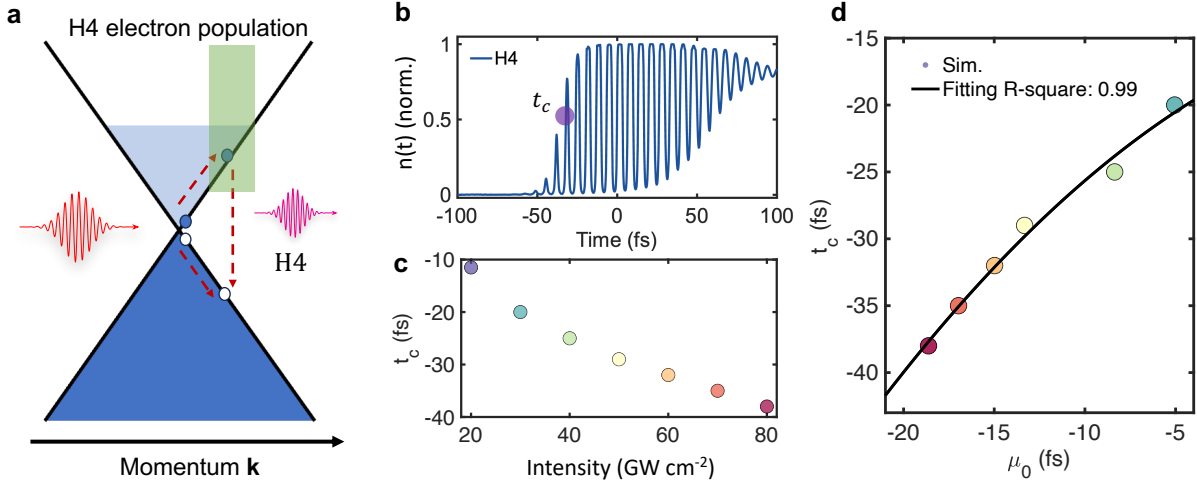


Figure 5. **Analysis of Dirac electron population dynamics via emission time shift.** **a**, Electron dynamics associated with fourth harmonic generation. The green shaded area indicates the region in momentum space where electron population contributes to H4 generation as the bandgap energy there corresponds to the H4 photon energy. **b**, Under excitation by a  $2 \mu\text{m}$  pulse with a peak intensity of  $70 \text{ GW cm}^{-2}$ , the H4 electron population oscillates as a function of propagation time. The time  $t_c$  marks the moment when half of the electrons in that region are excited. **c**, The absolute value of  $t_c$  increases with driving laser intensity, indicating an intensity-dependent excitation process. **d**, A strong correlation is observed between  $t_c$  (in the single-color  $2 \mu\text{m}$  excitation case) and  $\mu_0$  (in the two-color spectroscopy case). The color coding in panel d corresponds to that in panel c.

## CONCLUSION

In conclusion, our joint experimental and theoretical study has established an HHG-based all-optical approach to observe and quantify ultrafast depletion effects and carrier excitation dynamics in solids, which also yields absolute timing information. With respect to conventional bulk materials, such as ZnO, we found that the Dirac semimetal HOPG shows strong valence band population saturation due to its gapless nature even under moderate laser intensities ( $\sim 10^{10} \text{ W cm}^{-2}$ ), leading to half-filling in the vicinity of the Dirac point. We identified this effect as responsible for the observed  $\sim 17.5 \text{ fs}$  time shifts and the suppression of the harmonic emission in the later part of the driving laser pulse through Pauli blocking.

Our study demonstrates that gapless materials are subject to depletion effects and Pauli

blocking, leaving behind a sizable conduction band population and rendering harmonic generation processes nonparametric in nature. Petahertz optoelectronics, where optical manipulation of the material is performed on attosecond time scales, relies mainly on virtual charge carrier excitations and their reversibility<sup>8,33,34</sup>. In order to realize petahertz optoelectronics with full reversibility in gapless materials, pulse duration and peak intensity need to be limited such that Pauli blocking is avoided. Even if this cannot be achieved, gapless materials can nevertheless serve as an ultrafast optoelectronic switch where the presence or the absence of a pre-excitation pulse affects the efficiency of nonlinear processes through Pauli blocking on the significantly longer time scale of spontaneous emission. The nonparametric nature of HHG in gapless materials even at moderate intensities may also be helpful for generating upconverted light with nonclassical photon statistics due to the depletion effect, as recently predicted for gas-phase HHG<sup>35</sup>.

## METHODS

### Experimental setup

In the experiment, the fundamental ( $\omega_0$ ) pulse at 1980 nm is generated from a phase-stable optical parametric chirped pulse amplification (OPCPA) laser system operating at a repetition rate of 1 MHz (Class 5 Photonics White Dwarf<sup>36</sup>). The pulse duration of the  $\omega_0$  field measured by frequency-resolved optical gating (FROG) yields a full-width-at-half-maximum (FWHM) duration of approximately 60 fs ( $\sim 10$  optical cycles). The second harmonic ( $2\omega_0$ ) pulse was generated by focusing the fundamental beam into a  $\beta$ -barium borate (BBO) crystal under optimum phase-matching conditions. By adjusting the  $\omega_0$  power, we maintained the intensity ratio between the  $2\omega_0$  and  $\omega_0$  pulses at  $I_{2\omega_0}/I_{\omega_0} = 3\%$ . For HHG in HOPG, the  $\omega_0$  pulse energy was set between 1–5 nJ, while for ZnO, a higher energy of approximately 30 nJ was used.

The two-color interferometer setup was implemented by first separating the  $\omega_0$  and  $2\omega_0$  beams using a dichroic beam splitter. The relative delay between the two pulses was controlled via a piezo delay stage placed in the  $2\omega_0$  beam path. The two beams were then recombined by reflecting them off two mirrors back into the same dichroic beam splitter, with a slight lateral offset angle relative to the incoming paths, and subsequently directed

toward the sample for HHG. A parabolic mirror with  $f = 25$  mm focuses the light onto the HOPG sample (TipsNano) at an angle of incidence of 14 degrees. The beam size at the focus was measured using a knife-edge method, yielding an effective  $1/e^2$  radius of  $\approx 8.35 \mu\text{m}$  (see discussion and Fig. S1 in the Supplementary Information). We collect the harmonic light with a lens and send it to a Si-based spectrometer.

During the two-color delay scan, the piezo stage exhibited a minimal drift of less than 1 fs, which does not affect the accuracy of the delay-dependent measurements. Furthermore, to actively monitor and correct for any such drift, a portion of the combined  $\omega_0$ - $2\omega_0$  beam was directed into an additional BBO crystal to generate a reference SH signal. The resulting modulation arises from the interference between the newly generated SH signal from the  $\omega_0$  beam and the original  $2\omega_0$  pulse. This delay-dependent modulation serves as a timing reference, allowing for post-correction of any small delay drifts in the piezo stage.

The thickness of the reference ZnO crystal (FarView, (0001)) is 0.5 mm. Since the harmonics are measured in a reflection geometry on the crystal surface, nonlinear propagation effects associated with the crystal thickness do not influence our results.

### Semiconductor Bloch equations calculations

To describe the interaction of the two-color field and HOPG in the Dirac cone, we use the following one-dimensional semiconductor Bloch equations<sup>37,38</sup> (SBEs) centered around the Dirac cone:

$$\begin{aligned}
i\frac{\partial}{\partial t}p_k(t) &= \left[ \epsilon_k^c - \epsilon_k^v - i\frac{1}{T_2} + iE(t)\nabla_k \right] p_k(t) - (1 - f_k^c(t) - f_k^v(t)) d_k^{cv} E(t), \\
\frac{\partial}{\partial t}f_k^v(t) &= -2\text{Im} [d_k^{cv} E(t) (p_k^{vc}(t))^*] + \left[ -\frac{1}{T_1} + E(t)\nabla_k \right] f_k^v(t), \\
\frac{\partial}{\partial t}f_k^c(t) &= -2\text{Im} [d_k^{vc} E(t) (p_k^{cv}(t))^*] + \left[ -\frac{1}{T_1} + E(t)\nabla_k \right] f_k^c(t).
\end{aligned} \tag{1}$$

Here,  $p_k(t)$  represents a dimensionless polarization depending on time  $t$  and momentum  $k$ , induced by the time-dependent electric field  $E(t)$ . The indices  $v$  and  $c$  correspond to the valence band and conduction band, respectively.  $f_k^{c,v}(t)$  denotes the population of electrons (holes) in the conduction (valence) band. Here, we consider linear energy-momentum dispersion relation around Dirac cone with Fermi velocity  $v_F = 1 \times 10^6 \text{ m s}^{-1}$  describing a continuum ground state Dirac Hamiltonian. This approximation should be valid in our

regime where the laser-driven electrons only move near the Dirac cone. The transition dipole moments (TDMs) are calculated as  $d_k^{\nu c} = 1/(2|k|)$ <sup>39</sup> (see Fig. S3 in the Supplementary Information). We set the phenomenological interband polarization decoherence time to one optical cycle of the 2  $\mu\text{m}$  driving laser field  $T_2 = 6.6$  fs, and the relaxation time for intraband current to  $T_1 = 13$  ps. This consideration is valid since the relaxation is generally long and ranges from few hundred femtosecond to picosecond in graphene and is less sensitive to the results<sup>40,41</sup>. Band structure and TDM for ZnO crystal along the  $\Gamma$ -M direction are shown in Fig. S4 of the Supplementary Information (for details see the Supplementary Information). The calculations are performed with dense  $k$ -grid of size 200, using a time step of 2.4 as and according to the experimental parameters. The yield of the harmonics for the two-color case are calculated with two-color delay steps of  $\sim 0.33$  fs.

The HHG spectrum is computed as<sup>37</sup>

$$S_{\text{HHG}}(\omega) \sim \left| \int_{-\infty}^{\infty} [J_{\text{inter}}(t) + J_{\text{intra}}(t)] e^{i\omega t} dt \right|^2, \quad (2)$$

where

$$J_{\text{inter}}(t) = \frac{d}{dt} \int d_k^{\nu c} \cdot (p_k(t))^* dk + \text{c.c.} \quad (3)$$

and

$$J_{\text{intra}}(t) = \sum_{\lambda=c,\nu} \int \nu_k^\lambda f_k^\lambda(t) dk \quad (4)$$

denote the interband and intraband contributions to the HHG yield, respectively.  $\nu_k^\lambda = \nabla_k \epsilon_k^\lambda$  represents the group velocity of the electrons and holes in the corresponding bands.

### Analytical form of population dynamics

For a theoretical analysis of saturation and electron population dynamics, we begin by considering the *non-depleted* excitation rate of electrons from the valence band to the conduction band. According to Fermi's golden rule, this excitation rate at a given crystal momentum  $k$  and time  $t$  can be expressed as

$$w_0(k, t) \sim \frac{2\pi}{\hbar} |\langle \psi_c | \mathbf{E}(t) \cdot \nabla_k | \psi_v \rangle|^2 = 2\pi |\mathbf{E}(t) \cdot \mathbf{d}_{cv}(k)|^2. \quad (5)$$

The total excitation rate integrated over the Brillouin zone is then given by

$$w(t) = \int w_0(k, t) dk = 2\pi E^2(t) \int |\mathbf{d}_{cv}(k)|^2 dk. \quad (6)$$

Let  $P(t)$  denote the total conduction band electron population at time  $t$ . The evolution of this population in discrete time steps  $t_n \rightarrow t_{n+1}$  can be described by

$$P(t_{n+1}) = P(t_n) + (1 - P(t_n))w(t_n)dt - P(t_n)w(t_n)dt, \quad (7)$$

$$\frac{P(t_{n+1}) - P(t_n)}{1 - 2P(t_n)} = w(t_n)dt. \quad (8)$$

Transitioning to the continuous-time limit, we obtain the differential form

$$dP(t)/(1 - 2P(t)) = w(t)dt, \quad (9)$$

$$d \ln(1 - 2P(t)) = -2w(t)dt. \quad (10)$$

Integrating yields the electron population as a function of time,

$$P(t) = \frac{1 - e^{-\int_0^t 2w(\tau) d\tau}}{2}. \quad (11)$$

The actual (depleted) instantaneous excitation rate is given by

$$w_{\text{depletion}}(t) = dP(t)/dt = e^{-\int_0^t 2w(\tau) d\tau} \cdot w(t). \quad (12)$$

For interband-driven high-harmonic generation (HHG), the emitted harmonic intensity is proportional to the instantaneous excitation rate,  $I_{\text{HH}}(t) \sim w_{\text{depletion}}(t)$ .

## DATA AVAILABILITY

The data that support the plots within this paper and other findings of this study are available from the authors upon request.

## CODE AVAILABILITY

The codes that support the findings of this study are available from the authors upon request.

## **AUTHOR CONTRIBUTIONS**

Z. C. and C. G. contributed equally to this work.

M. K. and M. F. C. conceived and supervised the project, joined by O. N. in the later stage of the project. Z. C. built the experimental setup and performed the measurements. C. G. performed initial simulations. Z. C. carried out the theory calculations and C. G. and O. N. performed independent supplemental calculations. Z. C. and C. G. wrote the initial manuscript. All authors contributed to the interpretation of the results and to the preparation of the final manuscript.

## **CORRESPONDING AUTHORS**

Correspondence to Michael Krüger or Marcelo F. Ciappina.

## **ACKNOWLEDGMENTS**

We thank M. Ivanov, M. Segev, Q. Yan and Y. Wu for insightful discussions and U. Leonhardt and L. M. Procopio for providing specialized equipment. Z. C., C. G., I. N., D. K., M. F. C and M. K. acknowledge the Guangdong Technion – Israel Institute of Technology (GTIIT) and Technion Seed Grant Program for enabling their collaboration and joint research. Z. C., I. N., D. K., M. F. C and M. K. thank the Helen Diller Quantum Center at the Technion for partial financial support. M. F. C. acknowledges support by the National Key Research and Development Program of China (Grant No. 2023YFA1407100), Guangdong Province Science and Technology Major Project (Future functional materials under extreme conditions - 2021B0301030005) and the Guangdong Natural Science Foundation (General Program project No. 2023A1515010871).

## **ETHICS DECLARATIONS**

The authors declare no competing interests.

---

[1] Boyd, R. W. *Nonlinear Optics, Third Edition* (Academic Press, 2008), 3 edn.

- [2] Ferray, M., L’Huillier, A., Li, X. F., Lompre, L. A., Mainfray, G. & Manus, C. Multiple-harmonic conversion of 1064 nm radiation in rare gases. *J. Phys. B: At. Mol. Opt. Phys* **21**, L31 (1988).
- [3] McPherson, A., Gibson, G., Jara, H., Johann, U., Luk, T. S., McIntyre, I. A., Boyer, K. & Rhodes, C. K. Studies of multiphoton production of vacuum-ultraviolet radiation in the rare gases. *J. Opt. Soc. Am. B* **4**, 595–601 (1987).
- [4] Lewenstein, M., Balcou, P., Ivanov, M. Y., L’Huillier, A. & Corkum, P. B. Theory of high-harmonic generation by low-frequency laser fields. *Phys. Rev. A* **49**, 2117–2132 (1994).
- [5] Ghimire, S., DiChiara, A. D., Sistrunk, E., Agostini, P., DiMauro, L. F. & Reis, D. A. Observation of high-order harmonic generation in a bulk crystal. *Nat. Phys.* **7**, 138–141 (2011).
- [6] Vampa, G., Hammond, T. J., Thiré, N., Schmidt, B. E., Légaré, F., McDonald, C. R., Brabec, T. & Corkum, P. B. Linking high harmonics from gases and solids. *Nature* **522**, 462–464 (2015).
- [7] Ghimire, S. & Reis, D. A. High-harmonic generation from solids. *Nat. Phys.* **15**, 10–16 (2019).
- [8] Borsch, M., Meierhofer, M., Huber, R. & Kira, M. Lightwave electronics in condensed matter. *Nat. Rev. Mater.* **8**, 668–687 (2023).
- [9] Heide, C., Kobayashi, Y., Haque, S. R. U. & Ghimire, S. Ultrafast high-harmonic spectroscopy of solids. *Nat. Phys.* **20**, 1546–1557 (2024).
- [10] Schafer, K. J. & Kulander, K. C. High harmonic generation from ultrafast pump lasers. *Phys. Rev. Lett.* **78**, 638–641 (1997).
- [11] Shin, H. J., Lee, D. G., Cha, Y. H., Hong, K. H. & Nam, C. H. Generation of nonadiabatic blueshift of high harmonics in an intense femtosecond laser field. *Phys. Rev. Lett.* **83**, 2544–2547 (1999).
- [12] Rae, S. C., Burnett, K. & Cooper, J. Generation and propagation of high-order harmonics in a rapidly ionizing medium. *Phys. Rev. A* **50**, 3438–3446 (1994).
- [13] Gaarde, M. B., Tate, J. L. & Schafer, K. J. Macroscopic aspects of attosecond pulse generation. *J. Phys. B: At. Mol. Opt. Phys.* **41**, 132001 (2008).
- [14] Wang, Z., Park, H., Lai, Y. H., Xu, J., Blaga, C. I., Yang, F., Agostini, P. & DiMauro, L. F. The roles of photo-carrier doping and driving wavelength in high harmonic generation from a semiconductor. *Nat. Commun.* **8**, 1686 (2017).

- [15] Cheng, Y., Hong, H., Zhao, H., Wu, C., Pan, Y., Liu, C., Zuo, Y., Zhang, Z., Xie, J., Wang, J., Yu, D., Ye, Y., Meng, S. & Liu, K. Ultrafast optical modulation of harmonic generation in two-dimensional materials. *Nano Lett.* **20**, 8053–8058 (2020).
- [16] Heide, C., Kobayashi, Y., Johnson, A. C., Liu, F., Heinz, T. F., Reis, D. A. & Ghimire, S. Probing electron-hole coherence in strongly driven 2D materials using high-harmonic generation. *Optica* **9**, 512–516 (2022).
- [17] van Essen, P. J., Nie, Z., de Keijzer, B. & Kraus, P. M. Toward complete all-optical intensity modulation of high-harmonic generation from solids. *ACS Photonics* **11**, 1832–1843 (2024).
- [18] Pappis, J. & Blum, S. L. Properties of pyrolytic graphite. *J. Am. Ceram. Soc.* **44**, 592–597 (1961).
- [19] Blackman, L. C. F. & Ubbelohde, A. R. J. P. Stress recrystallization of graphite. *Proc. R. Soc. Lond. A Math. Phys. Sci.* **266**, 20–32 (1962).
- [20] Dresselhaus, M. S. & Dresselhaus, G. Intercalation compounds of graphite. *Adv. Phys.* **51**, 1–186 (2002).
- [21] Potamianos, D., Schnitzenbaumer, M., Lemell, C., Scigalla, P., Libisch, F., Schock-Schmidtke, E., Haimerl, M., Schröder, C., Schäffer, M., Kühle, J. T., Riemensberger, J., Eberle, K., Cui, Y., Kleineberg, U., Burgdörfer, J., Barth, J. V., Feulner, P., Allegretti, F. & Kienberger, R. Attosecond chronoscopy of the photoemission near a bandgap of a single-element layered dielectric. *Sci. Adv.* **10**, eado0073 (2024).
- [22] Zhou, S., Gweon, G.-H., Graf, J., Fedorov, A., Spataru, C., Diehl, R., Kopelevich, Y., Lee, D.-H., Louie, S. G. & Lanzara, A. First direct observation of Dirac fermions in graphite. *Nat. Phys.* **2**, 595–599 (2006).
- [23] Kumar, N., Kumar, J., Gerstenkorn, C., Wang, R., Chiu, H.-Y., Smirl, A. L. & Zhao, H. Third harmonic generation in graphene and few-layer graphite films. *Phys. Rev. B* **87**, 121406 (2013).
- [24] Bao, Q., Zhang, H., Wang, Y., Ni, Z., Yan, Y., Shen, Z. X., Loh, K. P. & Tang, D. Y. Atomic-layer graphene as a saturable absorber for ultrafast pulsed lasers. *Adv. Funct. Mater.* **19**, 3077–3083 (2009).
- [25] Cavalleri, A., Tóth, C., Siders, C. W., Squier, J., Ráksi, F., Forget, P. & Kieffer, J. Femtosecond structural dynamics in VO<sub>2</sub> during an ultrafast solid-solid phase transition. *Phys. Rev. Lett.* **87**, 237401 (2001).

- [26] Wegkamp, D. & Stähler, J. Ultrafast dynamics during the photoinduced phase transition in VO<sub>2</sub>. *Prog. Surf. Sci.* **90**, 464–502 (2015).
- [27] Nie, Z., Guery, L., Molinero, E., Juergens, P., Van Den Hooven, T., Wang, Y., Jimenez Galan, A., Planken, P., Silva, R. & Kraus, P. Following the nonthermal phase transition in niobium dioxide by time-resolved harmonic spectroscopy. *Phys. Rev. Lett.* **131**, 243201 (2023).
- [28] Vampa, G., You, Y. S., Liu, H., Ghimire, S. & Reis, D. A. Observation of backward high-harmonic emission from solids. *Opt. Express* **26**, 12210–12218 (2018).
- [29] Yoshikawa, N., Tamaya, T. & Tanaka, K. High-harmonic generation in graphene enhanced by elliptically polarized light excitation. *Science* **356**, 736–738 (2017).
- [30] Taucer, M., Hammond, T. J., Corkum, P. B., Vampa, G., Couture, C., Thiré, N., Schmidt, B. E., Légaré, F., Selvi, H., Unsuree, N., Hamilton, B., Echtermeyer, T. J. & Denecke, M. A. Nonperturbative harmonic generation in graphene from intense midinfrared pulsed light. *Phys. Rev. B* **96**, 195420 (2017).
- [31] Dudovich, N., Smirnova, O., Levesque, J., Mairesse, Y., Ivanov, M. Y., Villeneuve, D. M. & Corkum, P. B. Measuring and controlling the birth of attosecond XUV pulses. *Nat. Phys.* **2**, 781–786 (2006).
- [32] Vampa, G., McDonald, C. R., Orlando, G., Klug, D. D., Corkum, P. B. & Brabec, T. Theoretical analysis of high-harmonic generation in solids. *Phys. Rev. Lett.* **113**, 073901 (2014).
- [33] Sommer, A., Bothschafter, E. M., Sato, S. A., Jakubeit, C., Latka, T., Razskazovskaya, O., Fattahi, H., Jobst, M., Schweinberger, W., Shirvanyan, V., Yakovlev, V. S., Kienberger, R., Yabana, K., Karpowicz, N., Schultze, M. & Krausz, F. Attosecond nonlinear polarization and light-matter energy transfer in solids. *Nature* **534**, 86–90 (2016).
- [34] Boolakee, T., Heide, C., Garzón-Ramírez, A., Weber, H. B., Franco, I. & Hommelhoff, P. Light-field control of real and virtual charge carriers. *Nature* **605**, 251–255 (2022).
- [35] Stammer, P., Rivera-Dean, J., Maxwell, A. S., Lamprou, T., Argüello-Luengo, J., Tzallas, P., Ciappina, M. F. & Lewenstein, M. Entanglement and squeezing of the optical field modes in high harmonic generation. *Phys. Rev. Lett.* **132**, 143603 (2024).
- [36] Braatz, T., Zapolnova, E., Starosielec, S., Grguraš, I., Golz, T., Prandolini, M., Buss, J. H., Schulz, M. & Riedel, R. 1 MHz - dual channel, CEP stable, few-cycle OPCPA at 800nm and >1.7μm wavelength. In Schunemann, P. G. & Schepler, K. L. (eds.) *Nonlinear Frequency Generation and Conversion: Materials and Devices XX*, vol. 11670, 116700Z. International

- Society for Optics and Photonics (SPIE, 2021).
- [37] Golde, D., Meier, T. & Koch, S. W. High harmonics generated in semiconductor nanostructures by the coupled dynamics of optical inter- and intraband excitations. *Phys. Rev. B* **77**, 075330 (2008).
  - [38] Luu, T. T. & Wörner, H. J. High-order harmonic generation in solids: A unifying approach. *Phys. Rev. B* **94**, 115164 (2016).
  - [39] Al-Naib, I., Sipe, J. E. & Dignam, M. M. High harmonic generation in undoped graphene: Interplay of inter- and intraband dynamics. *Phys. Rev. B* **90**, 245423 (2014).
  - [40] Sato, S. A., Hirori, H., Sanari, Y., Kanemitsu, Y. & Rubio, A. High-order harmonic generation in graphene: Nonlinear coupling of intraband and interband transitions. *Phys. Rev. B* **103**, L041408 (2021).
  - [41] Liu, C., Zheng, Y., Zeng, Z. & Li, R. Driving-laser ellipticity dependence of high-order harmonic generation in graphene. *Phys. Rev. A* **97**, 063412 (2018).